



Dual-mechanism surface tension model for SPH-based simulation

Yuege Xiong¹ · Xiaokun Wang¹ · Yanrui Xu^{1,2} · Yalan Zhang³ · Jian Chang⁴ · Jianjun Zhang⁴ · Xiaojuan Ban³

Accepted: 9 May 2024

© The Author(s), under exclusive licence to Springer-Verlag GmbH Germany, part of Springer Nature 2024

Abstract

We present an innovative Lagrangian dual-mechanism model for simulating versatile surface tension phenomena, designed to replicate the intricate interplay of liquids with textured solid surfaces and the emergence of gas bubbles. This model synergistically merges the influence of inter-particle dynamics with global surface curvature, ensuring a harmonious balance between the intricacies of fluid motion and the imperative of surface area reduction. A cornerstone of our methodology is the incorporation of Laplace pressure differentials across fluid boundaries, enhancing interface stability and enabling the depiction of distinctive droplet oscillations driven by fluctuations in kinetic energy. Additionally, our model introduces a dual-scale smoothing kernel, meticulously engineered to resolve the subtle nuances of surface textures. The prowess of our model is exemplified in its ability to simulate superhydrophobic behaviors, underscoring its utility. Integrated within the smoothed particle hydrodynamics framework, our model offers efficient simulation performance, contributing a valuable tool to the field of fluid simulation.

Keywords Surface tension · Laplace pressure · Rough surface · Interface stability

1 Introduction

In nature, surface tension significantly influences fluid phenomena such as droplets [12], thin-film bubbles [18, 31], and splash crowns [1, 8]. The interaction of fluids with solid surfaces introduces complex behaviors like wetting and non-wetting [7, 37], influenced by the surface characteristics of the materials involved. This has spurred research in computer graphics [35] to accurately simulate these effects for improved visual realism.

Surface tension results from the unequal forces among molecules, modeled effectively in smoothed particle hydrodynamics (SPH) [23]. SPH uses macro-Lagrangian particles to simulate these molecular interactions, providing a framework for capturing fluid dynamics. Techniques such as the

inter-particle interaction force (IIF) within SPH address cohesion through a blend of attractive and repulsive forces. However, challenges like particle clustering and the need for larger computational resources can compromise the stability and smoothness of simulations (Fig. 1).

To enhance simulation fidelity, the continuum surface force (CSF) model [5] calculates surface tension through curvature. Yet, the CSF model struggles with accurately determining curvature near free surfaces due to kernel truncation, leading to errors and computational inefficiency [23, 39, 42]. These challenges underscore the ongoing need for advanced methods to simulate surface tension effectively within the confines of computer graphics research.

Furthermore, existing surface tension models have predominantly focused on fluid movement over smooth and continuous surfaces, limiting their ability to simulate specific hydrophilic or hydrophobic effects and notably failing to capture superhydrophobic behavior on rough surfaces. In real-world scenarios, contact surfaces often exhibit visible protrusions, indentations, or gaps, particularly pronounced at smaller scales. Regrettably, traditional models, reliant on larger-scale smoothing kernels [37], tend to overlook these intricate surface details.

To overcome these limitations, we introduce a dual-mechanism surface tension model in this paper, which

✉ Xiaokun Wang
wangxiaokun@ustb.edu.cn

Xiaojuan Ban
banxj@ustb.edu.cn

¹ School of Intelligence Science and Technology, University of Science and Technology Beijing, Beijing, China

² University of Groningen, Groningen, The Netherlands

³ University of Science and Technology Beijing, Beijing, China

⁴ Bournemouth University, Poole, UK



Fig. 1 Bubble coalescence

integrates particle interaction forces with curvature forces. Our approach differentiates between the dynamics of particles at the fluid surface and those within the bulk, while also addressing the issue of kernel truncation. Additionally, we incorporate a Laplace pressure adjustment based on the Young–Laplace equation to enhance the stability of fluid interfaces, facilitating the simulation of diverse surface tension phenomena and ensuring the minimization of surface area. A novel dual-scale smoothing kernel is proposed to recover the details lost at fluid–solid interfaces, enabling the successful simulation of Cassie [6] and Wenzel [34] phenomena, which represent two distinct states of fluid superhydrophobicity on various rough surfaces.

Our main contributions are as follows:

- Introduction of an accurate surface detection mechanism that identifies and corrects the truncated kernels of surface particles.
- Implementation of a Laplace pressure adjustment to enhance the interface stability of surface tension.
- Development of a dual-scale smoothing kernel designed to capture superhydrophobic phenomena by preserving detail on rough and discontinuous surfaces.

2 Related work

2.1 Particle-based methods

2.1.1 Inter-particle interaction force

Surface tension is a consequence of inter-molecular interactions at the microscopic level. Several studies have approximated these interactions by introducing attractive forces between neighboring particles [3, 9, 37, 38]. Clavet et al. [9] and Becker et al. [3] incorporated IIF within the SPH framework. Akinci et al. [1] and Huber et al. [14] combined cohesion and curvature forces to model surface tension. Despite their efforts, challenges remain, especially in simulating large surface tensions, leading to particle clustering and cobweb-like structures. Wang et al. [32] addressed these

issues by employing implicit incompressible SPH (IISPH) [16]. Yang et al. [37, 38] improved performance by using a larger smoothing kernel radius, though at the cost of increased computational complexity. Jeske et al. [18] proposed an implicit cohesion force to enhance surface tension stability but observed abnormal curvature at bubble adhesion surfaces.

2.1.2 Continuum surface force

Another approach to model surface tension in particle-based methods is through curvature, using the CSF method [1, 5, 23, 28, 39, 42]. Brackbill et al. [5] conceptualized surface tension as a volumetric force across interfaces. Morris et al. [22] and Muller et al. [23] simplified CSF for SPH. Akinci et al. [1] and Si et al. [28] achieved results comparable to IIF with proper tuning. However, CSF faces challenges in surface detection due to noisy kernel gradient normalization and curvature estimation sensitivity to sampling. Zorilla et al. [42] applied a method inspired by Monte Carlo integration for estimating local normals and curvatures. He et al. [12] took inspiration from the Cahn–Hilliard equation to derive a similar force for handling surface tension and air pressure.

2.2 Mesh-based methods

Mesh-based methods diverge from particle-based techniques by focusing on tracking the fluid surface to capture finer details. Zhang et al. [40] introduced a deformable surface mesh for droplets. Da et al. [11] developed a surface-only technique using triangle meshes for surface tension simulations. Zhu et al. [41] utilized non-manifold simplicial complexes for thin sheets and filaments. These methods find extensive application in simulating foam, bubbles, films [10, 17], and viscous sheets or threads [2, 4].

2.3 Hybrid methods

Hybrid methods combine Lagrangian particles and Eulerian grids to leverage the strengths of both approaches. Wang et al. [30] built on Zhu et al.’s work [41] in a Eulerian–Lagrangian

framework, using transition operators for fluid volume, sheet, and filament evolution. Hyde et al. [15] simulated liquid metals with high surface energy using material point method (MPM) and particle-in-cell (PIC). Chen et al. [7] introduced a MPM approach for Marangoni effects simulation due to tension gradients. Ruan et al. [26] developed a simplicial mesh membrane for strong surface tension-driven solid–fluid coupling. Xing et al. [36] proposed a novel position-based dynamics (PBD) framework approach with a local mesh structure for surface tension simulation.

We introduce a new particle-based surface tension model that combines the effects of particle interactions and surface curvature. By utilizing this dual-mechanism approach, we are able to consider both the intricacies of fluid motion and surface area minimization. The previously existing issue of estimation error in curvature is alleviated by incorporating Laplace pressure to correct the truncated surface particles. Furthermore, we introduce a dual-scale smoothing kernel to account for interactions between the fluid and rough solid surfaces that was previously overlooked.

3 SPH discretization

SPH is a Lagrangian framework used for simulating fluids by discretizing them into particles [23]. Each particle represents a portion of the fluid and carries properties such as mass, position, and velocity. In this paper, the subscript i and j are defined as target particle and neighbor particle separately. The Navier–Stokes equations govern the motion of fluids, and in the SPH context, they are expressed as follows for particle i :

$$\rho_i \frac{D\mathbf{v}_i}{Dt} = -\nabla p_i + \rho_i \nu \nabla^2 \mathbf{v}_i + \rho_i \mathbf{g} + \mathbf{F}_i^{\text{ST}}, \quad (1)$$

where ρ_i is the density, \mathbf{v}_i is the velocity, p_i is the pressure, ν is the kinematic viscosity coefficient, \mathbf{g} is the gravitational acceleration, and \mathbf{F}_i^{ST} represents surface tension forces acting on particle i .

In SPH, any scalar field ψ at the position \mathbf{x}_i of particle i is interpolated using contributions from all particles within a certain radius (defined by the smoothing length h), as given by:

$$\psi(\mathbf{x}_i) = \sum_j m_j \frac{\psi_j}{\rho_j} W(\mathbf{x}_i - \mathbf{x}_j, h), \quad (2)$$

where m_j is the mass and ψ_j/ρ_j is the value of the field per unit mass for particle j . W is the smoothing kernel function, which is often chosen to be a cubic spline as suggested by Monaghan [20] for its good balance between computational efficiency and accuracy.

According to Solenthaler et al. [29], the density of particle i can be approximated as:

$$\rho_i = \sum_j m_j W_{ij}, \quad (3)$$

where $W_{ij} = W(\mathbf{x}_i - \mathbf{x}_j, h)$.

The pressure for each particle is computed using the Tait equation [3], which ensures minimal density variations and is computationally efficient. As a common equation of state for SPH simulations of incompressible fluids, it can be expressed as:

$$p_i = B \left[\left(\frac{\rho_i}{\rho_0} \right)^7 - 1 \right], \quad (4)$$

where $B = \rho_0 c_s^2 / \gamma$ [24]. B is a stiffness coefficient related to the speed of sound c_s in the fluid and ρ_0 is the rest density of the fluid. The index is typically set to 7 for water-like fluids.

Pressure forces are then calculated to ensure fluid incompressibility and are given by:

$$-\frac{1}{\rho_i} \nabla p_i = -\sum_j m_j \left(\frac{p_i}{\rho_i^2} + \frac{p_j}{\rho_j^2} \right) \nabla W_{ij}. \quad (5)$$

This symmetrized version can preserve momentum. To enhance numerical stability and account for shock phenomena, artificial viscosity [21] is utilized as the viscosity force and computed as follows:

$$\nu \nabla^2 \mathbf{v}_i = \nu \sum_j m_j \left(\frac{\mathbf{v}_{ij} \cdot \mathbf{x}_{ij}}{|\mathbf{x}_{ij}|^2 + \epsilon^2} \right) \nabla W_{ij}, \quad (6)$$

where $\epsilon = 0.01h^2$. ϵ being a small value added to prevent singularity when particles are very close ($|\mathbf{x}_{ij}| = 0$). $\mathbf{v}_{ij} = \mathbf{v}_i - \mathbf{v}_j$ and $\mathbf{x}_{ij} = \mathbf{x}_i - \mathbf{x}_j$ represent the relative velocity and position.

4 Dual-mechanism surface tension

In this section, we delve into the intricate details of our dual-mechanism surface tension model, which stands out for its innovative approach to simulating fluid dynamics with enhanced precision and stability.

4.1 Surface particle detection and correction

A crucial component of our model is the precise identification and subsequent correction of surface particles, essential for preserving the accuracy of fluid simulations, particularly in regions near free surfaces or phase interfaces where the

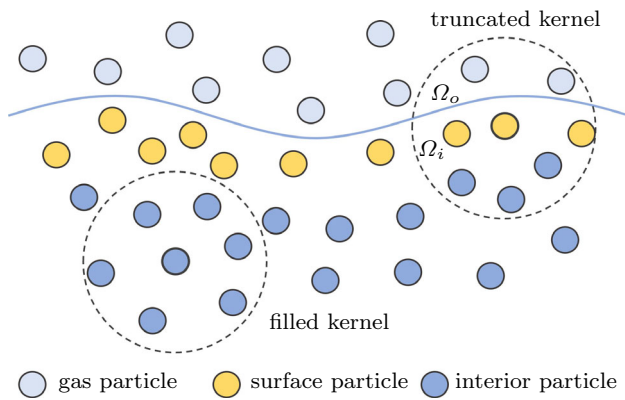


Fig. 2 Truncated kernel and filled kernel

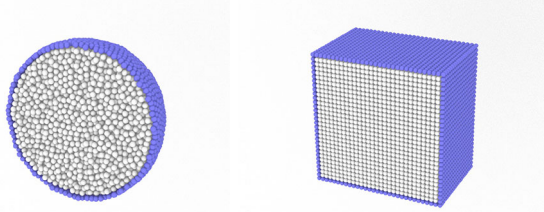


Fig. 3 Spherical and cubic surface detection. Surface particles and interior particles are shown in blue and white, respectively ($\eta = 0.88$)

distribution of particles is less dense. In such scenarios, conventional SPH methods might not accurately maintain the simulation's integrity, potentially leading to inaccuracies in the depiction of fluid dynamics and interactions. Specifically, at the interface or free surface, the diminished value of $\psi(\mathbf{x})$ in Eq. (2) becomes insufficient due to the truncation of the smoothing kernel, as illustrated in Fig. 2. This necessitates an independent correction for these particles.

In our surface tension model, updating particle labels at each time step is essential to accurately apply distinct algorithms for interior and surface particles. This necessitates a reliable and efficient technique for classifying particles. To achieve this, we utilize an advanced interpolation function inspired by Shepard's method [27], which effectively distinguishes between surface and interior particles. This approach computes a discriminant value D_i for each particle, employing a distance-weighted sum. For the weighting function, we select the Wendland kernel [33] due to it is a compactly supported function, which contribute to the robustness and efficiency of our surface detection process:

$$D_i = \begin{cases} \sum_j^N d_{ij} \xi_{ij} / \sum_j^N d_{ij} & d_{ij} \neq 0 \\ \xi_{ij} & d_{ij} = 0 \end{cases}, \quad (7)$$

where d_{ij} is the Cartesian distance. The term $\xi_{ij} = \frac{m_j}{\rho_j}$, where m_j is the mass and ρ_j is the density of neighbor particle j .

Equation (7) is refined as $D_i = \sum_j^N \xi_{ij} W_{ij}$. The value of D_i can be used to differentiate interior particles from surface particles by introducing a threshold η ($\eta < 1$). If $D_i > \eta$, particle i is defined as an interior particle; otherwise, it is categorized as a surface particle. The result of surface particle detection is shown in Fig. 3. We replace d_{ij} with a distance weighting factor derived from the Wendland kernel [33], defined by:

$$W_{ij} = \begin{cases} \frac{21}{16\pi h^3} \left(1 - \frac{x_{ij}}{2h}\right)^4 \left(\frac{2x_{ij}}{h} + 1\right) & x_{ij} \leq h \\ 0 & x_{ij} > h \end{cases}. \quad (8)$$

Here, $x_{ij} = \mathbf{x}_i - \mathbf{x}_j$ represents the distance between particles i and j , and $h = 0.08$ is the smoothing length. This kernel smoothly diminishes with distance, ensuring contributions from neighboring particles decrease as they move further away.

For surface particles, the kernel encompasses both gas and fluid particles, necessitating a division into inside area Ω_i and outside area Ω_o at the phase boundary, illustrated in Fig. 2. The pressure force for surface particles is then adjusted to account for external gas pressure, comprising environmental pressure (p_{env}) and the Laplace pressure jump (Δp) at curved gas–liquid interfaces. The modified pressure force equation is:

$$-\frac{1}{\rho_i} \nabla p_i = - \sum_{\Omega_i} m_j \left(\frac{p_i}{\rho_i^2} + \frac{p_j}{\rho_j^2} \right) \nabla W_{ij} - \sum_{\Omega_o} m_j \left(\frac{p_i}{\rho_i^2} + \frac{\Delta p + p_{\text{env}}}{\rho_j^2} \right) \nabla W_{ij}. \quad (9)$$

For interior particles, where p_{env} and Δp effectively become zero and contributions from particles in Ω_o are not considered, the pressure force calculation reverts to the symmetric form as per the standard SPH methodology. This distinction in pressure force calculation for surface versus interior particles enhances the accuracy and stability of simulations, especially in capturing the dynamics at fluid interfaces and free surfaces.

4.2 Laplace pressure jump

The Laplace pressure jump (Δp), incorporated in Eq. (9), plays a crucial role in our surface tension model, especially noticeable at sharp free surfaces. This pressure differential is attributed to surface tension forces and is quantitatively determined by the curvature of the fluid surface, as articulated by the Young–Laplace equation:

$$\Delta p = -\gamma \nabla \cdot \mathbf{n} = 2\gamma H = \gamma \left(\frac{1}{R_1} + \frac{1}{R_2} \right), \quad (10)$$

where γ represents the surface tension coefficient, $\hat{\mathbf{n}}$ denotes the normalized normal vector to the surface, and H signifies the mean curvature with R_1 and R_2 being the principal curvature radii of the surface.

To compute the normal vector \mathbf{n}_i at the surface, we employ the following formulation:

$$\mathbf{n}_i = -\frac{1}{D_i} \sum_j \frac{m_j^2}{\rho_j^2} W_{ij} \sum_j \nabla W_{ij}, \quad (11)$$

where W_{ij} is the smoothing kernel function as defined in Eq. (8) and D_i is the discriminant value used to differentiate surface particles, ensuring that the calculation accounts for the truncated kernel effect. This approach, through the factor $\frac{1}{D_i}$, scales the normal vector computation for surface particles, effectively mitigating the noise typically encountered in surface normal calculations. The normalized form of the normal vector is expressed as $\hat{\mathbf{n}}_i$, which is essential for accurately determining the curvature and, consequently, the Laplace pressure jump across the fluid interface. Our experimental results validate the efficacy of this method in enhancing the precision of surface-related computations within the SPH framework.

To enhance the precision of gradient interpolation within our model, we incorporate a renormalization technique inspired by Oger et al. [24], which adjusts the gradient of the kernel function ∇W . This adjustment is crucial for maintaining the accuracy of calculated gradients, particularly in the context of surface tension modeling where precise curvature measurements are essential. The renormalized kernel gradient $\nabla^R W$ is defined as:

$$\nabla^R W(\mathbf{x}_i - \mathbf{x}_j) = R(\mathbf{x})^{-1} \nabla W(\mathbf{x}_i - \mathbf{x}_j), \quad (12)$$

where $R(\mathbf{x})$ is a correction matrix of dimension $d \times d$, with d representing the spatial dimensionality of the problem. This matrix corrects the gradient based on the spatial configuration of neighboring particles, ensuring that the interpolation of gradients remains consistent even in complex flow scenarios.

For illustrative purposes, the two-dimensional form of the correction matrix $R(\mathbf{x})$ is presented, showcasing how the matrix elements are computed based on the spatial differences between particle positions and the gradients of the smoothing kernel weighted by ω_j , which represents the volume equivalent of particle j :

$$\begin{pmatrix} \sum_j^N (\mathbf{x}_j^1 - \mathbf{x}_i^1) \nabla W(\mathbf{x}_{ij}) \omega_j & \sum_j^N (\mathbf{x}_j^1 - \mathbf{x}_i^1) \nabla W(\mathbf{x}_{ij}) \omega_j \\ \sum_j^N (\mathbf{x}_j^2 - \mathbf{x}_i^2) \nabla W(\mathbf{x}_{ij}) \omega_j & \sum_j^N (\mathbf{x}_j^2 - \mathbf{x}_i^2) \nabla W(\mathbf{x}_{ij}) \omega_j \end{pmatrix}. \quad (13)$$

The curvature tensor \mathbf{K}_i , a pivotal component in calculating surface curvature and, by extension, the Laplace pressure jump, is derived using this renormalized kernel gradient:

$$\mathbf{K}_i = \sum_j^N \omega_j \hat{\mathbf{n}}_{ij} \otimes \nabla^R W_{ij}, \quad (14)$$

where $\hat{\mathbf{n}}_{ij}$ is the difference in normalized normal vectors between particles i and j .

To calculate the mean curvature as referenced in Eq. (10), we need to determine the principal curvature radii. Drawing from shell theory in solid mechanics [25] and adapting for our fluid simulation context, we establish a local coordinate system using normalized orthogonal tangent vectors and the normal vector from Eq. (11). The basis vectors for this system are $\mathbf{L} = (\hat{\mathbf{n}}, \hat{\mathbf{t}}_i^1, \hat{\mathbf{t}}_i^2)$. The first tangent vector $\hat{\mathbf{t}}_i^1$ is computed as follows:

$$\hat{\mathbf{t}}_i^1 = \begin{cases} \hat{\mathbf{n}} \times (0, 1, 0) & \text{if } \|\hat{\mathbf{n}} \times (0, 1, 0)\| > 0.01 \\ \hat{\mathbf{n}} \times (1, 0, 0) & \text{else} \end{cases}, \quad (15)$$

to ensure orthogonality with $\hat{\mathbf{n}}_i$.

The second tangent vector $\hat{\mathbf{t}}_i^2$ is obtained via the cross product $\hat{\mathbf{t}}_i^2 = \hat{\mathbf{n}} \times \hat{\mathbf{t}}_i^1$, ensuring a mutually orthogonal set of vectors. The curvature tensor \mathbf{K}_i in Eq. (14) is then transformed from the Cartesian to the local coordinate system using the transformation matrix \mathbf{T}_i , as defined by:

$$\tilde{\mathbf{K}}_i = \mathbf{T}_i^T \mathbf{K}_i \mathbf{T}_i, \quad (16)$$

where \mathbf{T}_i aligns the curvature tensor with the local coordinate system established by \mathbf{L} . This transformation facilitates the accurate calculation of curvature by considering the local geometry of the fluid surface.

To deduce the principal curvatures $\frac{1}{R_1}$ and $\frac{1}{R_2}$, we evaluate the eigenvalues of the transformed curvature tensor $\tilde{\mathbf{K}}_i$, which has been adjusted to a 2D form by omitting components along the normal direction. The Laplace pressure jump Δp_i is then adjusted to account for these curvatures, enhancing the model's stability and accuracy in simulating surface tension effects:

$$\Delta p_i = \frac{\gamma_i}{2} \left(\frac{1}{R_{1i}} + \frac{1}{R_{2i}} \right) \left(\frac{1}{D_i} + 1 \right). \quad (17)$$

4.3 Combined surface tension force

Our model introduces a nuanced approach to the computation of surface tension forces by incorporating a dual-scale smoothing kernel. This method addresses the limitations identified in previous studies, such as those by Yang et al. [37], who utilized a larger smoothing kernel to enhance the

stability of surface tension effects but at the cost of losing fine details due to the expanded neighbor search radius. Directly reducing the kernel size could lead to inaccuracies from insufficient neighbor particles. To alleviate these issues, we propose an interaction force that leverages both the standard and a reduced-scale smoothing kernel, as described by:

$$\mathbf{F}_i^{\text{interaction}} = \sum_j^N (a_{ij} W(\mathbf{x}_{ij}, h) - b_{ij} W(\mathbf{x}_{ij}, 0.7h)) \frac{\mathbf{x}_{ij}}{|\mathbf{x}_{ij}|}, \quad (18)$$

where W is defined as $\cos\left(\frac{3\pi}{2h} |\mathbf{x}_{ij}|\right)$, with a_{ij} and b_{ij} representing coefficients for the standard and reduced-scale kernels, respectively. This dual-scale approach allows for the preservation of detail while maintaining the stability improvements seen with larger kernels.

To illustrate the effectiveness of this approach, we simulate the behavior of droplets on various textured surfaces, modeling superhydrophobic phenomena as described by Cassie [6] and Wenzel [34]. In the Cassie state, droplets are supported above the surface by micro- or nano-structures, creating air pockets beneath them, whereas in the Wenzel state, the liquid fully wets the textured surface, filling the grooves. These distinct behaviors are crucial for understanding and simulating superhydrophobic surfaces, and our model's capability to accurately represent both states is demonstrated in Fig. 4, showing the versatility and precision of our dual-scale kernel method in capturing complex surface interactions.

To accurately represent the intricate behaviors of fluids interacting with textured surfaces, such as those depicted in Fig. 4, we employ a mathematical model to construct sinusoidal and dual-sinusoidal surfaces. The height function for these surfaces is defined as:

$$h(x) = \frac{A}{2} \sin\left(\frac{2\pi x}{T}\right) + 0.05 \quad (19)$$

where $A = 0.3$ and $T = 0.5$ denote the amplitude and period of the sinusoidal wave, respectively, and h represents the height of the surface features (Fig. 5).

While the interaction force, defined by Eq. 18, is adept at simulating fluid behaviors on both smooth and textured surfaces, it does not inherently ensure the minimization of surface area, a fundamental characteristic of surface tension.

Additionally, early stages of the simulation may exhibit perturbations in kinetic energy, a challenge commonly encountered with IIF methods. To address these issues, we introduce a curvature force component, computed using the principal curvature radii determined in Sect. 4.2, as follows:

$$\mathbf{F}_i^{\text{curvature}} = \gamma \mathbf{n}_i \left(\frac{1}{R_{1i}} + \frac{1}{R_{2i}} \right). \quad (20)$$

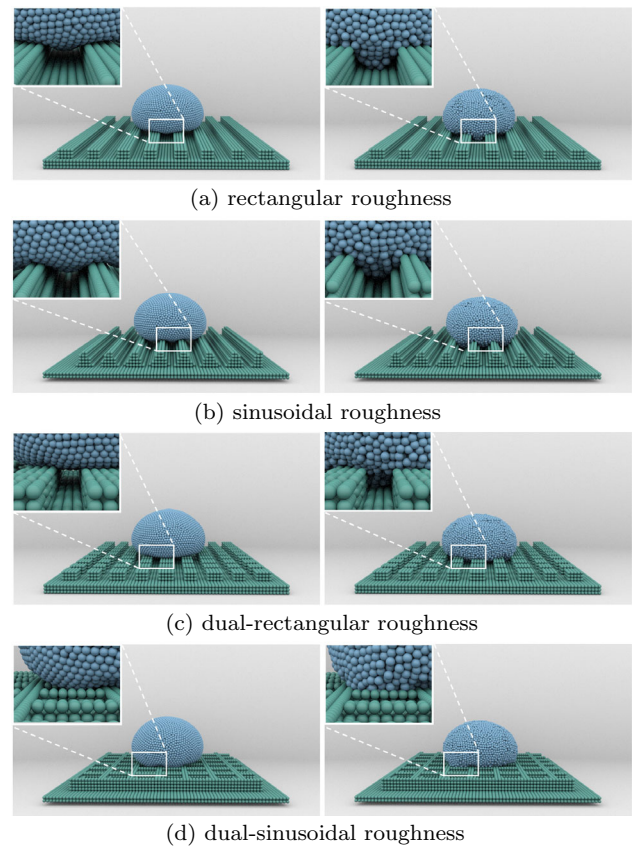


Fig. 4 Superhydrophobic effect on diverse types of rough surface. We set the droplet to fall on surface. The Cassie and Wenzel states correspond to the left and right sides of the subfigure, respectively. In the Cassie state, we can observe light passing through the gap; in the Wenzel state, droplet sinks into the grooves

This force component is nullified for particles on flat surfaces by making Eq. (20) equal to zero, where the curvature radii are infinite, and is progressively amplified for particles on more curved surfaces. Figure 6 illustrates the model's capability to accurately replicate the behavior of fluids under the influence of surface tension.

The overall surface tension force \mathbf{F}_i^{ST} in Eq. (1) for each particle is computed by combining the interaction force $\mathbf{F}_i^{\text{interaction}}$ with the curvature force $\mathbf{F}_i^{\text{curvature}}$, as integrated within the weakly compressible SPH (WCSPH) framework. This comprehensive approach, detailed in our algorithm (Algorithm 1), allows for the simulation of complex fluid dynamics, ensuring realistic depiction of surface tension phenomena in fluid simulations (Fig. 7).

5 Experiments

We implement the algorithm by using Taichi [13] and Python programming language on the Nvidia GeForce RTX 4060 GPU. We conducted the following experiments to demon-



Fig. 5 Stream ribbon of wine

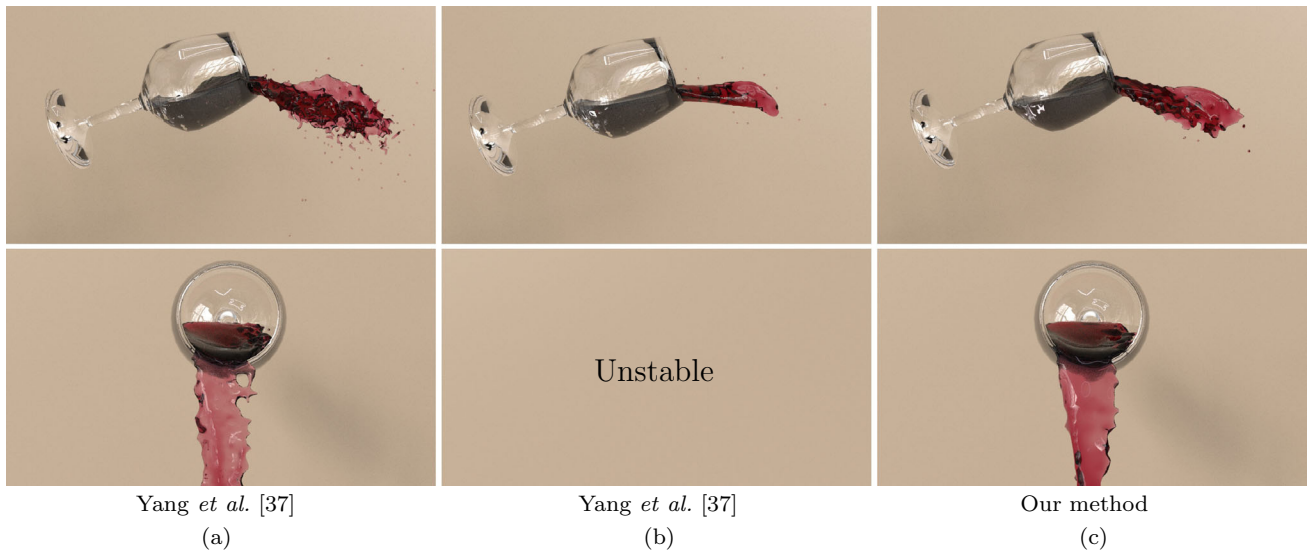


Fig. 6 Comparison of surface area minimization. We compare our method with Yang *et al.* [37] in same frame. **c** Significantly reduces particle splashing compared to **(a)** by minimizing the surface area under

the same scale of surface tension. We attempted to address this issue by enhancing the surface tension; yet, it led to an unstable simulation outcome in **(b)**



Fig. 7 Dew on the palm leaf

strate the effectiveness and superiority of our method. Surface reconstruction and rendering are performed using the Mantra engine in Houdini. The performance of all examples is summarized in Table 1.

5.1 Droplet oscillation

Figure 8 illustrates a specific phenomenon of cubic droplet oscillation in the zero-gravity environment, which is pri-

marily driven by surface tension. The droplet only directly contracts into a spherical shape in Yang *et al.*'s [37] method or retains a rhombic shape in Si *et al.*'s [28] method. Our method can capture a regular shape transformation process, as shown in Fig. 8c. This effect is characterized by setting $\gamma = 100$ and the coefficient $a = 30$. As a benchmark for evaluating surface tension models, the kinetic energy associated with the droplet's oscillation is plotted against time steps, depicted in

Algorithm 1 Simulation Loop**Preparation**

search neighboring particles
 update density ρ_i
 calculate viscosity force and gravity (6)

Detection

update detection value D_i (7)
 compute pressure force for interior particles (5)

Surface Tension

compute $\mathbf{F}_i^{\text{interaction}}$ (18)
 update normal vector (11)
 normalized kernel gradient $\nabla^R W$ (12)
 compute curvature tensor \mathbf{K}_i (14)
 compute principal curvature radius R_1, R_2 from $\tilde{\mathbf{K}}_i$ (16)
 compute curvature force $\mathbf{F}_i^{\text{curvature}}$ (20)

Pressure Correction

update Laplace pressure Δp_i (17)
 correct pressure force for surface particle (9)
 update velocity and position

Fig. 9, serving as an indicator of our model's capability to accurately incorporate Laplace pressure adjustments.

Figure 9a focuses on the impact of Laplace pressure in the context of CSF methods, where surface tension is solely

accounted for by curvature forces. Here, the kinetic energy exhibits a gradual decline, punctuated by clear, periodic oscillations corresponding to the cubic droplet's deformation, highlighted by the green line in the graph.

Subsequently, Fig. 9b juxtaposes our method with that of Yang et al. [37] and Si et al. [28], offering a comparative analysis. Unlike our model, both Yang et al.'s and Si et al.'s approaches cannot capture distinct oscillatory behavior, and an unexplained disturbance is noticeable in the early simulation stages, underscoring the advantages of our enhanced surface tension treatment. Our simulation result in Figs. 8 and 9 is consistent with those of Lundgren et al. [19].

5.2 Stream ribbon

This experiment simulates a scenario where red wine is poured from a tilted glass, creating a stream ribbon of wine flowing through the air, as depicted in Fig. 5. We adjusted the tension coefficient γ to 40 to observe the effects on the fluid's surface tension. A comparison experiment is conducted in this scenario to showcase the surface area minimization,

Table 1 Efficiency performance on examples

Examples	Particles	Steps/frame	Msec/frame	Frames/frame
Oscillation	43K	8	14.4	69.4
Stream ribbon	82K	8	16.8	59.5
Bubble	23K	10	11.8	84.7
Rough surface	12K	5	12.5	80.0
Palm leaf	2K	10	9.1	109.9
Impaled droplet	2K	5	8.7	114.9



(a) Yang et al. [37].



(b) Si et al. [28].



(c) Our method.

Fig. 8 Droplet oscillation in zero gravity

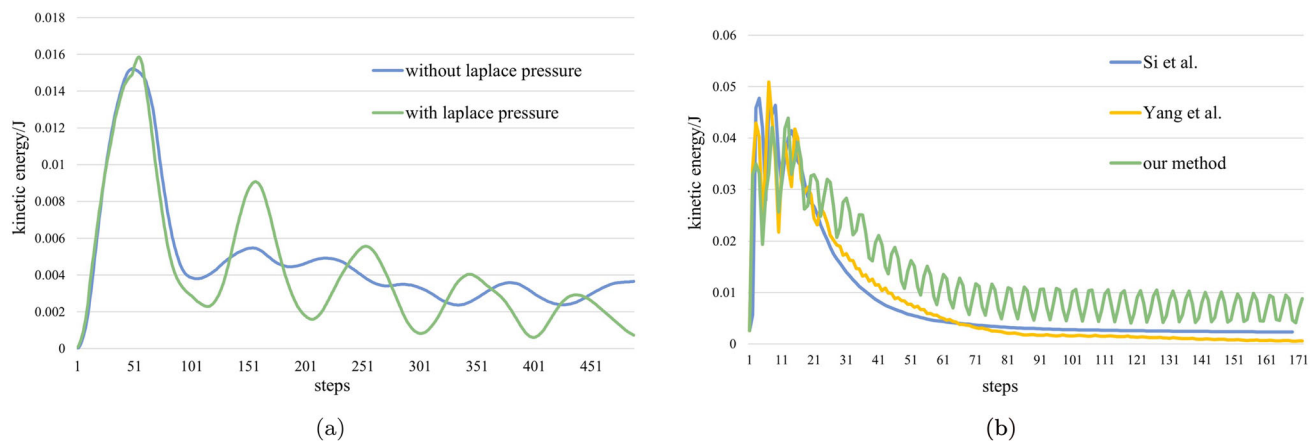


Fig. 9 Kinetic energy of droplet oscillation as a function of time step. **a** Comparison of Laplace pressure on CSF methods. **b** Comparison of our method Si et al. [28] and Yang et al. [37] method

as shown in Fig. 6. The simulation on the right side apparently reduces particle splashing and demonstrates a smoother effect, suggesting that our dual-mechanism model effectively minimizes the fluid surface area. From a frontal perspective, our approach can successfully preserve the integrity of the thin-film structure, preventing any ruptures. This experiment underscores the ability of our method to accurately represent slender fluid features and highlights the enhanced stability of our surface tension model in handling delicate fluid dynamics.

5.3 Bubble coalescence

Our model adeptly simulates bubble dynamics by robustly handling the gas–liquid interface via Laplace pressure adjustments. Within this setup, the bubble’s film is composed of fluid particles, while the interior is filled with gas particles. Initially, bubbles of differing sizes are placed at a distance from each other. Driven by the inter-particle forces, they gradually move toward one another and agglomerate to achieve an equilibrium state as illustrated in Fig. 1. The parameters set for this simulation were $\gamma = 100$, with coefficients $a = 100$ and $b = 10$, respectively, showcasing our model’s capability to simulate complex bubble interactions.

5.4 Superhydrophobic surface

Figure 4 shows four distinct rough surfaces characterized by pronounced protrusions and indentations, designed to mimic superhydrophobic textures at the microscale. These surfaces serve as a basis for simulating the superhydrophobic effect, successfully capturing both Cassie and Wenzel wetting states. The employment of a dual-scale smoothing kernel allows for a detailed depiction of droplets interacting with surface grooves. The simulation parameters for the Cassie state were set to $a = 130$ and $b = 10$, while for the

Wenzel state, they were adjusted to $a = 130$ and $b = 120$, facilitating the accurate representation of these complex wetting phenomena.

5.5 Dew on the palm leaf

To verify our method in a more realistic scenario, we visualize a droplet landing on a palm leaf, emulating the behavior of dew being enveloped by an elastic membrane. The simulation captures the droplet’s stable slide across the leaf’s surface and its eventual detachment upon reaching a over-wide gap. This setup highlights our model’s proficiency in managing fluid interactions with discontinuous surfaces and intricate boundaries, providing a realistic portrayal of dew accumulation and movement on foliage. The simulation parameters were set to $a = 130$, $b = 20$, and $\gamma = 10$, demonstrating the model’s effectiveness in rendering detailed fluid–surface interactions.

5.6 Impaled droplet

To evaluate the stability of droplet in contact with sharp objects, we conduct the experiment, as depicted in Fig. 10. The droplet falls from the apex of the cone and becomes pierced to form a ring structure. To emphasize the impact of surface tension, we strategically reduced the influence of gravity after reaching 500 frames in the simulation, allowing surface tension to play a dominant role. The water ring subsequently breaks into smaller droplets due to surface tension. Comparing our method to Si et al. [28], upon observation in Fig. 10a, obvious unstable splashes are generated when the water ring breaks and shrinks into droplets. Figure 10b shows that droplets can stably break into smaller size using our method. The parameters for this simulation were configured as $a = 40$, $b = 0$, and $\gamma = 100$, displaying the stability of fluids upon collision with sharp surfaces.

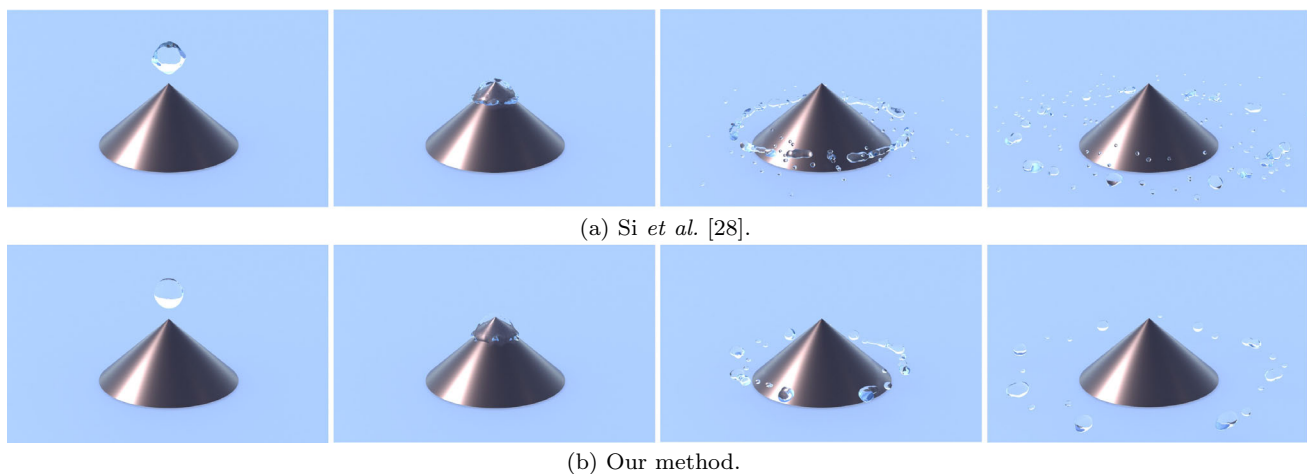


Fig. 10 Impaled droplet

6 Conclusion and discussion

In this work, we have introduced a new dual-mechanism model for simulating surface tension, effectively combining particle interaction forces with curvature forces. This integration allows for the accurate depiction of a wide range of behaviors, while also maintaining surface stability and minimizing surface area. Our method overcomes common issues related to curvature computation inaccuracies by categorizing particles as either surface or interior types, and it addresses the truncated kernel problem at fluid interfaces through the application of Laplace pressure corrections.

Our model's stability and efficacy have been thoroughly evaluated, both numerically and visually, demonstrating significant improvements over existing techniques. Additionally, we have expanded the realm of surface tension simulations to include interactions with specially textured rough surfaces, an aspect often overlooked in previous research. The implementation of a dual-scale smoothing kernel in our model recovers critical surface details, enabling the simulation of superhydrophobic phenomena, which represents a novel contribution to the field.

Despite these advancements, our current model employs an explicit approach for calculating Laplace pressure, which may restrict the time step size in large-scale simulations. Besides, with the introduction of Laplace pressure, additional kinetic energy is introduced, leading to deviations from an entirely zero energy curve. In the future research, we will delve into implicit formulations of Laplace pressure to seamlessly integrate them with implicit pressure solvers, strengthening the scalability and usability of our model. Furthermore, our focus will shift toward exploring the interactions between fluids and porous materials, exploring phenomena such as fluid penetration and absorption. This

exploration aims to enhance the capabilities and realism of our surface tension model even further.

Acknowledgements This research was funded by the National Key Research and Development Program of China (No.2022ZD0118001), the National Natural Science Foundation of China (Nos.62376025, 62332017, U22A2022), and the Guangdong Basic and Applied Basic Research Foundation (Nos.2023A1515030177, 2022A1515110350, 2021A1515012285).

References

1. Akinci, N., Akinci, G., Teschner, M.: Versatile surface tension and adhesion for SPH fluids. *ACM Trans. Graph. TOG* **32**(6), 1–8 (2013)
2. Batty, C., Uribe, A., Audoly, B., Grinspun, E.: Discrete viscous sheets. *ACM Trans. Graph. TOG* **31**(4), 1–7 (2012)
3. Becker, M., Teschner, M.: Weakly compressible SPH for free surface flows. In: *ACM Siggraph/Eurographics Symposium on Computer Animation* (2007)
4. Bergou, M., Audoly, B., Vouga, E., Wardetzky, M., Grinspun, E.: Discrete viscous threads. *ACM Trans. Graph. TOG* **29**(4), 1–10 (2010)
5. Brackbill, J.U., Kothe, D.B., Zemach, C.: A continuum method for modeling surface tension. *J. Comput. Phys.* **100**(2), 335–354 (1992)
6. Cassie, A., Baxter, S.: Wettability of porous surfaces. *Trans. Faraday Soc.* **40**, 546–551 (1944)
7. Chen, J., Kala, V., Marquez-Razon, A., Gueidon, E., Hyde, D.A., Teran, J.: A momentum-conserving implicit material point method for surface tension with contact angles and spatial gradients. *ACM Trans. Graph. TOG* **40**(4), 1–16 (2021)
8. Chen, Y.L., Meier, J., Solenthaler, B., Azevedo, V.C.: An extended cut-cell method for sub-grid liquids tracking with surface tension. *ACM Trans. Graph. TOG* **39**(6), 1–13 (2020)
9. Clavet, S., Beaudoin, P., Poulin, P.: Particle-based viscoelastic fluid simulation. In: *Proceedings of the 2005 ACM SIGGRAPH/Eurographics Symposium on Computer Animation*, pp. 219–228 (2005)
10. Da, F., Batty, C., Wojtan, C., Grinspun, E.: Double bubbles sans toil and trouble: discrete circulation-preserving vortex sheets for soap films and foams. *ACM Trans. Graph. TOG* **34**(4), 1–9 (2015)

11. Da, F., Hahn, D., Batty, C., Wojtan, C., Grinspun, E.: Surface-only liquids. *ACM Trans. Graph. TOG* **35**(4), 1–12 (2016)
12. He, X., Wang, H., Zhang, F., Wang, H., Wang, G., Zhou, K.: Robust simulation of sparsely sampled thin features in SPH-based free surface flows. *ACM Trans. Graph. TOG* **34**(1), 1–9 (2014)
13. Hu, Y., Li, T.M., Anderson, L., Ragan-Kelley, J., Durand, F.: Taichi: a language for high-performance computation on spatially sparse data structures. *ACM Trans. Graph. TOG* **38**(6), 201 (2019)
14. Huber, M., Reinhardt, S., Weiskopf, D., Eberhardt, B.: Evaluation of surface tension models for SPH-based fluid animations using a benchmark test. In: *VRIPHYS*, pp. 41–50 (2015)
15. Hyde, D.A., Gagniere, S.W., Marquez-Razon, A., Teran, J.: An implicit updated Lagrangian formulation for liquids with large surface energy. *ACM Trans. Graph. TOG* **39**(6), 1–13 (2020)
16. Ihmsen, M., Cornelis, J., Solenthaler, B., Horvath, C., Teschner, M.: Implicit incompressible SPH. *IEEE Trans. Vis. Comput. Graph.* **20**(3), 426–435 (2014)
17. Ishida, S., Synak, P., Narita, F., Hachisuka, T., Wojtan, C.: A model for soap film dynamics with evolving thickness. *ACM Trans. Graph. TOG* **39**(4), 31–1 (2020)
18. Jeske, S.R., Westhofen, L., Löschner, F., Fernández-fernández, J.A., Bender, J.: Implicit surface tension for SPH fluid simulation. *ACM Trans. Graph.* **43**(1), 1–14 (2023)
19. Lundgren, T., Mansour, N.: Oscillations of drops in zero gravity with weak viscous effects. *J. Fluid Mech.* **194**, 479–510 (1988)
20. Monaghan, J.J.: Simulating free surface flows with SPH. *J. Comput. Phys.* **110**(2), 399–406 (1994)
21. Monaghan, J.J.: Smoothed particle hydrodynamics. *Rep. Prog. Phys.* **68**(8), 1703 (2005)
22. Morris, J.P.: Simulating surface tension with smoothed particle hydrodynamics. *Int. J. Numer. Methods Fluids* **33**(3), 333–353 (2000)
23. Müller, M., Charypar, D., Gross, M.: Particle-based fluid simulation for interactive applications. In: *Proceedings of the 2003 ACM SIGGRAPH/Eurographics Symposium on Computer Animation*, pp. 154–159 (2003)
24. Oger, G., Doring, M., Alessandrini, B., Ferrant, P.: An improved SPH method: towards higher order convergence. *J. Comput. Phys.* **225**(2), 1472–1492 (2007)
25. Plateau, J.A.F.: *Statique expérimentale et théorique des liquides soumis aux seules forces moléculaires*, vol. 2. Gauthier-Villars, Paris (1873)
26. Ruan, L., Liu, J., Zhu, B., Sueda, S., Wang, B., Chen, B.: Solid–fluid interaction with surface-tension-dominant contact. *ACM Trans. Graph. TOG* **40**(4), 1–12 (2021)
27. Shepard, D.: A two-dimensional interpolation function for irregularly-spaced data. In: *Proceedings of the 1968 23rd ACM National Conference*, pp. 517–524 (1968)
28. Si, W., Liao, X., Qian, Y., Wang, Q., Heng, P.A.: Versatile numerical fractures removal for SPH-based free surface liquids. *Comput. Graph.* **81**, 1–8 (2019)
29. Solenthaler, B., Pajarola, R.: Density contrast SPH interfaces. In: *ACM Siggraph/Eurographics Symposium on Computer Animation* (2008)
30. Wang, H., Jin, Y., Luo, A., Yang, X., Zhu, B.: Codimensional surface tension flow using moving-least-squares particles. *ACM Trans. Graph. TOG* **39**(4), 1–42 (2020)
31. Wang, M., Deng, Y., Kong, X., Prasad, A.H., Xiong, S., Zhu, B.: Thin-film smoothed particle hydrodynamics fluid. *ACM Trans. Graph. TOG* **40**(4), 1–16 (2021)
32. Wang, X.K., Ban, X.J., Zhang, Y.L., Liu, S.N., Ye, P.F.: Surface tension model based on implicit incompressible smoothed particle hydrodynamics for fluid simulation. *J. Comput. Sci. Technol.* **32**, 1186–1197 (2017)
33. Wendland, H.: Piecewise polynomial, positive definite and compactly supported radial functions of minimal degree. *Adv. Comput. Math.* **4**, 389–396 (1995)
34. Wenzel, R.N.: Resistance of solid surfaces to wetting by water. *Ind. Eng. Chem.* **28**(8), 988–994 (1936)
35. Wang, X., Xu, Y., Liu, S., Ren, B., Kosinka, J., Telea, A.C., Wang, J., Song, C., Chang, J., Li, C., Zhang, J.J., Ban, X.: Physics-based fluid simulation in computer graphics: survey, research trends, and challenges. *Comput. Vis. Media CVM* (2024). <https://doi.org/10.1007/s41095-023-0368-y>
36. Xing, J., Ruan, L., Wang, B., Zhu, B., Chen, B.: Position-based surface tension flow. *ACM Trans. Graph. TOG* **41**(6), 1–12 (2022)
37. Yang, T., Lin, M., Martin, R.R., Chang, J., Hu, S.: Versatile interactions at interfaces for SPH-based simulations. In: *Eurographics/ACM SIGGRAPH Symposium on Computer Animation* (2016), pp. 57–66. Association for Computing Machinery (2016)
38. Yang, T., Martin, R.R., Lin, M.C., Chang, J., Hu, S.M.: Pairwise force SPH model for real-time multi-interaction applications. *IEEE Trans. Vis. Comput. Graph.* **23**(10), 2235–2247 (2017)
39. Zhang, M.: Simulation of surface tension in 2D and 3D with smoothed particle hydrodynamics method. *J. Comput. Phys.* **229**(19), 7238–7259 (2010)
40. Zhang, Y., Wang, H., Wang, S., Tong, Y., Zhou, K.: A deformable surface model for real-time water drop animation. *IEEE Trans. Vis. Comput. Graph.* **18**(8), 1281–1289 (2011)
41. Zhu, B., Quigley, E., Cong, M., Solomon, J., Fedkiw, R.: Codimensional surface tension flow on simplicial complexes. *ACM Trans. Graph. TOG* **33**(4), 1–11 (2014)
42. Zorilla, F., Ritter, M., Sappl, J., Rauch, W., Harders, M.: Accelerating surface tension calculation in SPH via particle classification and Monte Carlo integration. *Computers* **9**(2), 23 (2020)

Publisher's Note Springer Nature remains neutral with regard to jurisdictional claims in published maps and institutional affiliations.

Springer Nature or its licensor (e.g. a society or other partner) holds exclusive rights to this article under a publishing agreement with the author(s) or other rightsholder(s); author self-archiving of the accepted manuscript version of this article is solely governed by the terms of such publishing agreement and applicable law.



Yuege Xiong is a postgraduate student at the School of Intelligence Science and Technology, University of Science and Technology Beijing. She received an undergraduate Diploma in Beijing University of Technology, in 2022. Her research field is computer graphics, especially physics-based fluid simulation.



Jian Chang is a professor in the National Centre for Computer Animation at Bournemouth University, UK. He received his Ph.D. degree in computer graphics from Bournemouth University in 2007. His research interests include physics based modeling (deformation and fluid), motion synthesis, virtual reality (surgery simulation), and novel HCI (eye tracking, gesture control, and haptics).



Xiaokun Wang is an associate professor in Intelligence Science and Technology, University of Science and Technology Beijing, China. He received a Ph.D. degree in computer science and technology from the University of Science and Technology Beijing, in 2017. He is currently working at the National Centre for Computer Animation at Bournemouth University funded by the EU's Horizon 2020 Marie Curie Individual Fellowship. His research interests include computer graphics, virtual

reality, and human-computer interaction.



Jianjun Zhang is a professor and director of the UK National Centre for Computer Animation Research at Bournemouth University. His research interests include 3D computer animation, virtual human modeling, virtual reality, and physics-based simulation.



Yanrui Xu is a Ph.D. student at Bernoulli Institute, University of Groningen and the School of Intelligence Science and Technology, University of Science and Technology Beijing. He received his Master's degree from the University of Science and Technology Beijing in 2020. His research interests include physics-based fluid simulation.



Xiaojuan Ban is a professor at the School of Intelligence Science and Technology, University of Science and Technology Beijing. She is the leader of the Artificial Intelligence and 3D Visualization Group at University of Science and Technology Beijing, China. She received her Ph.D. degree in control theory and control engineering from the University of Science and Technology Beijing. Her research interests include computer graphics, artificial intelligence, human-computer interaction, big data analysis, and 3D visualization.



Yalan Zhang is a lecture at the School of Intelligence Science and Technology, University of Science and Technology Beijing. She received her Ph.D. degree in computer science and technology from the University of Science and Technology Beijing. Her research interests include computer graphics, intelligence simulation, and 3D visualization.